A&A manuscript no.
(will be inserted by hand later)

Your thesaurus codes are:
08(08.05.1;08.06.2;08.13.3),09(09.10.1)

Embedded infrared clusters and H_2 nebulosities in S233IR *

A. Porras[1], I. Cruz-González[2] and L. Salas[3]

[1] Instituto Nacional de Astrofísica, Optica y Electrónica,
Apdo. Postal 216, Puebla, Pue. 72000, México.
aporras@inaoep.mx

[2] Instituto de Astronomía, UNAM, Apdo. Postal 70-264, C.U., México, D.F. 04510, México.
irene@astroscu.unam.mx

[3] Instituto de Astronomía, UNAM, Apdo. Postal 877, Ensenada, B.C. 22830, México.
salas@astrosen.unam.mx

Received .... / Accepted ....

Abstract. We present an infrared photometric imaging study of the star formation region associated to IRAS05358+3543, hereafter designated S233IR. Several manifestations of star formation activity are present in S233IR: maser, molecular outflow, GMC core, YSOs, young stellar clusters and an IRAS source. The paper includes photometric J, H, K and H_2 (2.12 μm) images and scanning Fabry-Perot observations to study H_2 kinematics in a $3.6' \times 3.6'$field. Two distinct young stellar clusters separated by 0.5 pc are found in the region, one being redder than the other with a difference of $\sim$7 mag in average extinction; we address the issue of whether this is indicative of an age difference and/or a different spatial location in the GMC. We found a collection of PMS objects and several H_2 nebulosities associated to the younger and redder NE cluster produced by shocked gas. Two deeply embedded jet-counter-jet structures produced by shocked H_2 gas are detected near the core of the molecular outflow. Possible exciting source candidates of the molecular outflow and H_2 are discussed. The velocity field of H_2 gas shows that the bulk of the intensity within -36.9 to 2.3 km/s, individual spectra of H_2 nebulosities show peak velocities consistent with the rest velocity of the GMC and H_2O masers peak velocities. Luminosity function histograms are used to obtain a crude age estimate for each cluster, 1 Myr for the SW one and 0.3 Myr for the NE cluster, indicating at least two

Send offprint requests to: I. Cruz-González

* Based on observations obtained at the Observatorio Astronómico Nacional at San Pedro Mártir, B.C., México.

Correspondence to: irene@astroscu.unam.mx

star formation stages. Finally, the stellar IMF for sources in the embedded clusters in S233IR is briefly addressed.

Key words: 08.05.1 – 08.06.2 – 08.13.3 – 09.10.1

---

1. Introduction

We have been studying in the NIR young stellar clusters (YSCs) near HII regions and IRAS sources located along the Perseus Arm. Our aim is to derive extinction to individual stars, luminosity functions, cluster ages and individual stellar masses, with the main goal of studying the stellar mass distribution (IMF) of 45 YSCs in Perseus (Porras et al. 2000). In order to describe our methodology and analysis we present here the study of an embedded SFR near S233, hereafter designated S233IR. We selected this region for a detailed study because it also contains H_2 nebulosities that resemble Herbig-Haro objects, as some of the regions in our Perseus survey (e.g. S187IR, Salas et al. 1998).

We observed the region surrounding the IRAS source 05358+3543 (α_{1950} = 05^h 35^m 48.8^s, $\delta_{1950} = +35°43'41''$), which has been associated to the HII region S233 (e.g. Chan et al. 1996; Henning et al. 1992) based on its position by Israel & Felli (1978). As is shown in Fig. 1, S233 is part of a giant molecular cloud located in the Perseus Arm that includes four HII regions: S231, S232, S233, S235, with S233 being the smallest and closer to IRAS05358+3543. The association of the IRAS source and the HII regions is supported by CO maps of the GMC by Heyer et al. (1996) over an area of $\sim$ 3°×2° in the sky. A maximum peak of V_{LSR} $\sim$-17 km/s from the spatially averaged spectra over the entire region is detected, which agrees with previous observations by Snell et al. 1990 for a region of $6'\times6'$centered on the IRAS source.

We adopt a conservative value of 1.8 kpc to the IRAS source and its associated star forming region. From the spectral type of the HII regions exciting source, values of 1.6±0.50 kpc for S235, 2.3±0.7 kpc for S231 (Fich & Blitz 1984) and 2.3±0.7 kpc for S233 (Chan & Fich 1995), have been reported. Nevertheless, the 1.8 kpc value (Evans & Blair 1981) has been widely used (e.g. Wilking et al. 1989; Snell et al. 1990; Henning et al. 1992; Hodapp 1994; Schreyer et al. 1996), since it represents a mean spectroscopic distance value to S235.

IRAS05358+3543 is a candidate for a star forming region according to several criteria (e.g. Wood & Churchwell 1989; Hughes & MacLeod 1989; Palagi et al. 1993) based on the IRAS observed fluxes. This is supported by maser detections in the region (see Fig. 1). VLA observations of H_2O maser by Tofani et al. (1995) with 0.1″position accuracy, show four emission peaks located to the NE of IRAS05358+3543. Also, an OH maser

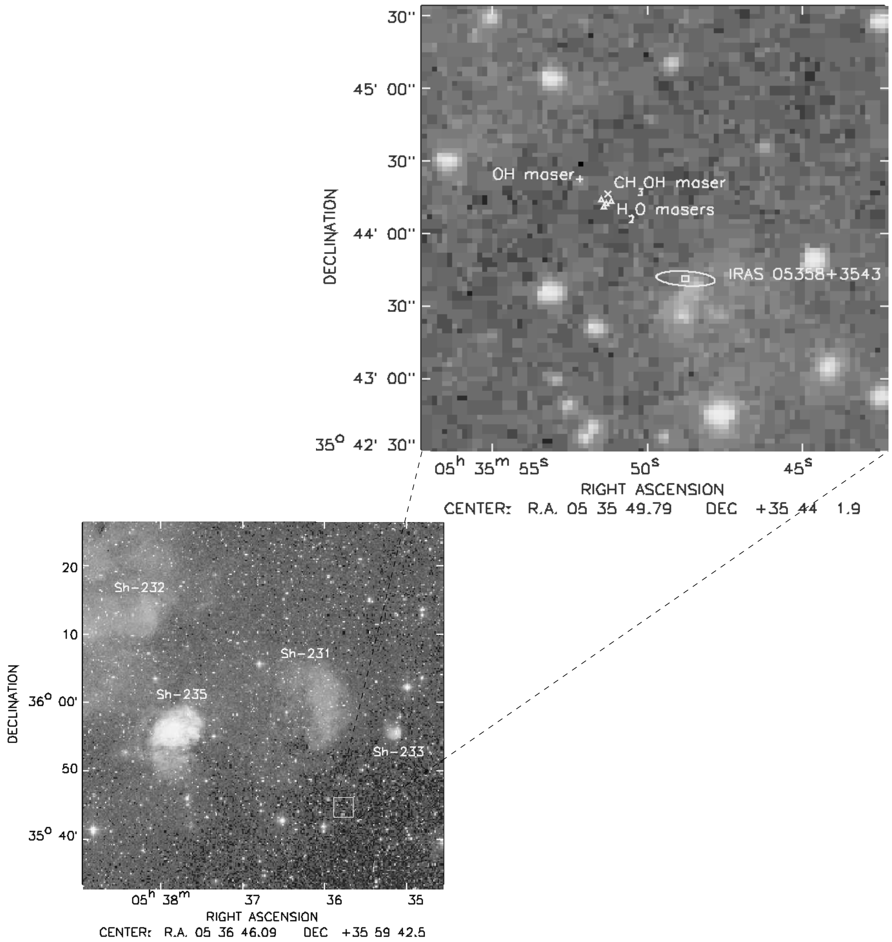

Fig. 1. Optical maps from the complex of Sharpless H II regions (from left to right) S232, S235, S231 and S233. The enlargement of the observed region includes the location of IRAS 05358+3543 with its error ellipse, and the positions of H_2O ($\triangle$), OH ($+$) and CH_3OH ($\times$) maser detections (Tofani et al. 1995; Wouterloot et al. 1988; Menten 1991).

detected by Wouterloot et al. 1988 (30″position accuracy) located to the NE of H_2O masers; while methanol maser emission observed by Menten 1991 (HPBW=5′) lies closer to the H_2O masers.

Different observations of molecular lines towards S233IR have been reported and show that the associated region is a core source in the GMC (e.g. ^{13}CO detected by Casoli et al. 1986 and Wilking et al. 1989; ^{12}CO by Wouterloot & Brand 1989; CS (2-1) by Bronfman et al. 1996; HCO^+ (1-0) by Richards et al. 1987 and Schreyer et al. 1996; NH_3 (1,1) and (2,2) by Schreyer et al. 1996. Casoli et al. 1996 estimated that the GMC associated with S231, S233 and S235 has a gas column density $N_{H_2} = 55 \times 10^{20}$ cm^{-2} and mass $M_{H_2} = 450$ M$_\odot$.

S233IR was observed at K' (7′×3′field) by Hodapp (1994), with limiting magnitude 17.5. He notes the presence of an embedded young stellar cluster, two bright stars with associated nebulosity and nebular features probably excited by shocks that resemble HH objects. However, Wilking et al. (1989) failed to detect mm continuum sources in the region.

Several star formation tracers are found in S233IR: masers, molecular outflows, high density cores, stellar clusters and an IRAS source, making it an excellent candidate for a near-IR study. In this paper we present JHK photometric observations (§2 and §3) and a study of molecular hydrogen emission (§4). Several infrared H_2 nebulosities are detected with characteristics of shock features. Velocity maps of H_2 gas are studied via Fabry-Perot observations and are also compared to kinematic radio studies. Possible exciting sources of these H_2 nebulosities, fluxes, morphology and velocities suggest that S233IR contains two jet-counter-jet deeply embedded Herbig-Haro objects (§5). We show that S233IR is a singular example of two young embedded clusters at a different evolutionary state. The luminosity function and IMF of cluster stars are briefly addressed (§5).

2. Observations

2.1. Direct imaging

Observations were taken with the infrared camera CAMILA (Cruz-González et al. 1994) at the 2.1 m telescope in San Pedro Mártir, operated by the Observatorio Astronómico Nacional (OAN/SPM) in Baja California, México. Images were obtained under photometric conditions on 1997 January 24 through the broad-band filter K' (2.125 μm, $\Delta\lambda$=0.35 μm) [1], and narrow-band filter cK (2.26 μm, $\Delta\lambda$=0.06); and on January 27 through the broad-band filters J (1.20 μm, $\Delta\lambda$=0.28 μm) and H (1.60 μm, $\Delta\lambda$=0.27 μm), and narrow-band filter H_2 v=1-0 S(1) (2.122 μm, $\Delta\lambda$=0.02 μm). Five added object images were processed by subtracting a median-filtered image of four nearby sky frames taken with the same exposure times at adjacent positions to the object. The total integration times were 600 s, 600 s, 900 s, 900 s, and 600 s in J, H, K, H_2 and cK, respectively. The FWHM PSF of the images were 2.3″(J), 2.2″(H), 2.3″(K'), 2.2″(H_2) and 2.0″(cK). The plate scale of CAMILA was 0.84 ″/ pix. The images were flattened by low and high illumination sky flats obtained at sunset. The flux calibration was obtained by observing the UKIRT faint standard stars 18, 19 and 20. The position of the sources in the field is solved linearly from nine optically visible stars in the Digitized Sky Survey, and the resultant positional uncertainty is 1″. The continuum subtracted image of H_2 was obtained by estimating the continuum from a weighted average of the continuum K-filter and the H-filter, in order to have a better subtraction for blue objects.

[1] This is the Barr Associates filter known as Mauna Kea K'

A composite color image (JHK) of the region (see Fig. 2a) shows two distinct groups of stars, one of them at a north-east position (here on, NE cluster) being redder than the one at a south-west position (here on, SW cluster). The observed field, $3.67' \times 3.67'$, corresponds to 1.92×1.92 pc^2 at the adopted distance of 1.8 kpc, and the projected separation between clusters is $\sim 1'$ (0.52 pc). Also, as have been noted by Hodapp (1994), there are some nebular features probably produced by shock-excited gas (see §4).

2.2. Infrared Fabry-Perot

The observations were carried out at the f/4.5 Cassegrain focus of the same telescope at OAN/SPM. Images under photometric conditions were taken on 1998 October 3. The plate scale was the same as in broad band images and the seeing was $2.2''$(FWHM). A set of images was obtained at 26 etalon positions (channels) that scan a single order at 9.82 km s^{-1} per channel for H_2 v=1-0 S(1) (2.122 μm narrow filter). A complete instrumental setup description of the IR Fabry-Perot interferometer is presented in Salas et al. (1999).

The observing sequence consisted of alternative imaging of the region and a blank sky region $81''$ to the east for each etalon position. The telescope allowed that the on-source image was accurately positioned back within $1''$, eliminating re-centering problems. On-source and sky integration times were 60 s. The typical 1 σ noise in any image is 0.07 counts s^{-1} pixel^{-1}, while the intensity in extended emission regions of interest goes up 1.0 count/s/pixel. The 2.1332885 μm line of the Ar lamp was observed at each etalon position for calibration after the source and sky images, obtaining a velocity uncertainty of 0.5 km/s in the wavelength fit. A series of high and low illumination sky flats at each etalon position were obtained at sunset for flat-fielding.

3. Photometry and Results

3.1. Stellar photometry routines

The photometry of the infrared sources in the $3.6' \times 3.6'$ field was obtained with DAOPHOT routines (Landsman 1996) in IDL. DAOPHOT routines for stellar fields were adapted to our infrared images and allowed us to follow a consistent set of reduction routines, useful for any rich stellar field observed with CAMILA. A detailed description of the reduction procedure for IR clusters will be presented by Porras (2000). Point sources were identified with FIND routine, with the detection threshold set to 3σ above the local background. Due to the number of stars in the region we obtained photometry using the PSF fitting algorithm GETPSF. The PSF fitting radius was 3 pixels and the local sky annulus was set from 6 to 8 pixels. Magnitudes were transformed from the UKIRT to the homogenized

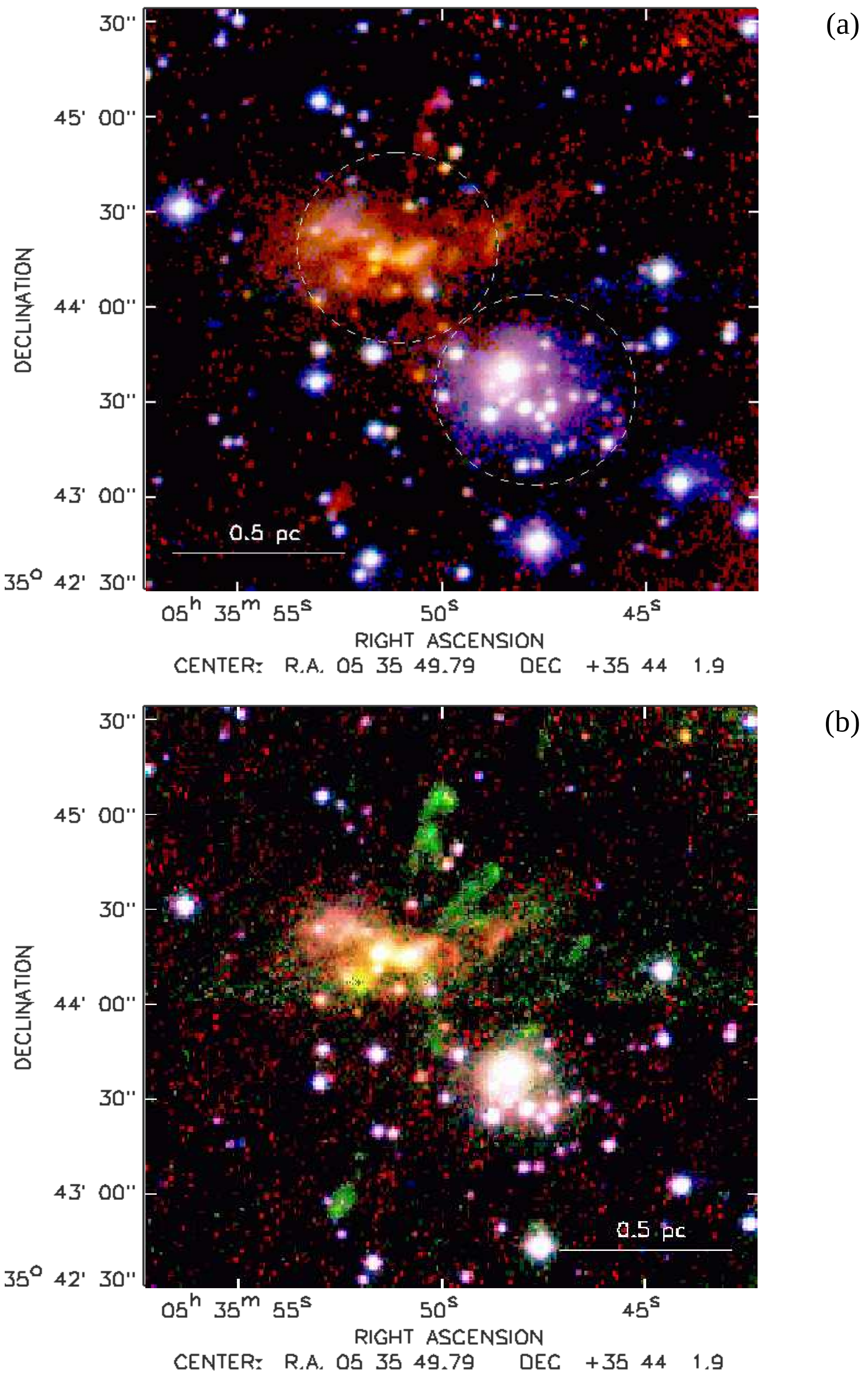

Fig. 2. Composite NIR color images of the region around IRAS05358+3543. **a** Shows emission in J (blue), H (green) and K' (red). This field covers $3.1' \times 3.1'$ which corresponds to 1.6 pc $\times$ 1.6 pc at D = 1.8 kpc. Two groups of stars (NE and SW clusters) are revealed, as well as several nebular features spread from North to South across the image, shown in red. Dashed circles of $1'$ in diameter are drawn around each cluster to clarify the location of the NE and SW clusters. **b** Shows emission in H (blue), H_2 (green) and cK (red). Note that H_2 nebulosities stand out in green.

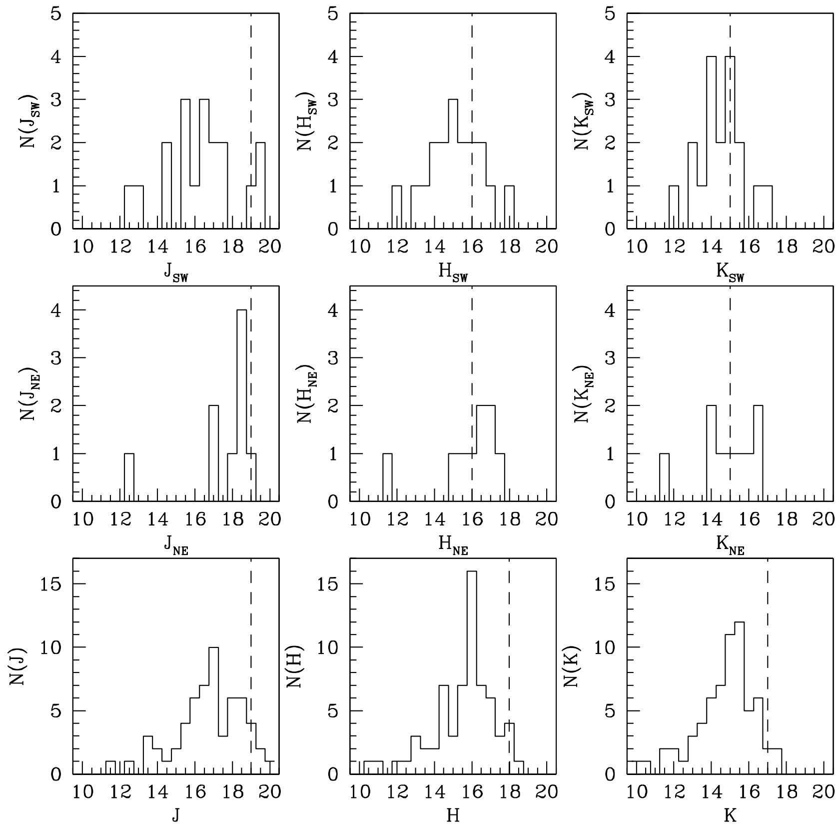

Fig. 3. Luminosity histograms at J, H and K for NE cluster, SW cluster and field stars (non-cluster). Completeness limits are represented by vertical broken lines.

Glass-Johnson system, using the transformation equations of Bessell & Brett (1988). The intrinsic error in the photometry is less than 7%. We used mean atmospheric extinction coefficients derived by Carrasco et al. (1991) for the observing site.

For the whole region, the differential completeness limits in magnitude are 19, 18 and 17 mag in the J, H and K' filters, respectively. They were obtained as the fraction of stars recovered via ADDSTAR within a magnitude bin in a histogram of stellar magnitudes.

In regions with strong nebulosity the differential completeness limits are 19, 16 and 15 in the J, H and K' filters, respectively. Thus in H and K' the gas component affects the completeness limit by $\sim$2 mag.

JHK luminosity histograms are presented in Fig. 3 for each cluster and field stars. The K-band histogram is quite similar to that obtained by Hodapp (1994) for S233. The strong similarities to the JHK histograms obtained by Carpenter et al. (1997) for the MonR2 region, reinforce that S233IR is also a young stellar cluster.

Table 1 includes photometric near-infrared data for 98 stars in S233IR. Note that 92 stars are detected in JHK and that sources IR 93 to IR 98 are quite red and undetected in J. Five of these red stars are likely members of the NE cluster, since they lie inside the 1' circle; while IR 98 lies outside the clusters. If so, the population clearly associated to clusters is of 20 and 15 stars in the SW and NE clusters, respectively. Coordinates were obtained using Skyview optical images using positions common to infrared sources to derive target positions in the usual way. The extinction A_V associated to each source is given in Col. (7) and the procedure to derive them is described in §3.3 below.

3.2. Color-Color Diagram

By examining the density of stars in the field, for the SW cluster we have chosen a $1'$diameter, which contains all blue stars without an optical counterpart around a density maxima. For a fair comparison of stellar populations, we have chosen a similar diameter for the NE cluster. The J-H/H-K diagram presented in Fig. 4 includes all the detected stars and shows a high population of YSOs. Main sequence stars (MS), affected by normal interstellar reddening, are located in the region between the two upper dotted lines in this diagram. Clear color differences between the two clusters are revealed (c.f. Fig. 2a), with NE cluster members as well as nebular gas being much redder.

OJO: By degrading spatial resolution we checked that colors were not affected significantly (<1%) by local background in regions with nebulosity.

Unusual colors are observed for IR 39 and IR 57. Source IR 39 (J-H=2.08, H-K=0.28) corresponds to an unresolved pair of stars located in the SW cluster, for which individual photometry is needed. IR 57 (J-H=1.48, H-K=0.18) is a very bright star located in the western edge of the observed field, surprisingly it does not have an optical counterpart and seems not to be related with any of the clusters. IR 23 is a deeply embedded MS star (J-H=2.53, H-K=0.99) not located in any of the clusters.

In each cluster we have counted the population of stars with near-IR excesses, i.e. those located to the right of the MS reddening line: 40% (6/15) for the NE cluster, 30% (6/20) for the SW cluster and 29% (15/51) for stars outside the two clusters. It should be noted that 5 sources in the NE cluster are not detected in the J-band so their J-H color is unknown while in H-K are extremely red. This may increase the percentage of IR-excess stars in the NE cluster. Also, we have only considered stars in the J-H/H-K diagram located above 1σ from the CTTS locus. We consider foreground stars (6) based on $A_V >$ 1.8, J-H $<$ 1 and H-K $<$ 0.4, which are omitted from our analysis.

Leaving flexible the parameter of roundness, IDL/DAOPHOT procedures can also find and calculate the photometry of objects that are not stellar. Such is the case of a pair of H_2 nebulosities N1 and N2 (see §4 below), for which photometric data was available. Their positions in the J-H/H-K diagram are quite distinct from stellar sources,

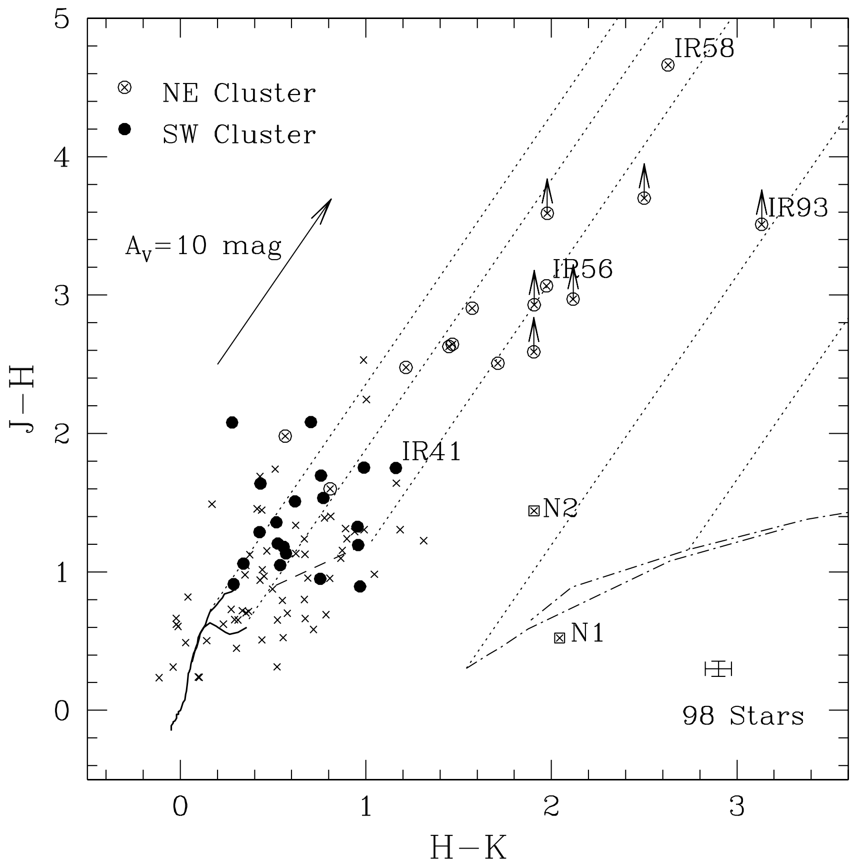

Fig. 4. Color-color diagram of the stars around IRAS05358+3543. The main sequence and red giant branch are drawn with solid lines (Bessell & Brett 1988). The dashed line shows the CTTS locus (Meyer 1996). The dotted lines follow the direction of the interstellar reddening vector A_V. We used different symbols for stars inside a circle of $1'$ in diameter centered in each of the two clusters, (•) for SW cluster members and (⊗) for NE cluster members, while field stars are shown as ×. Arrows indicate lower limits for stars without J counterpart. In the lower right part of the diagram, N1 and N2 show the location of the brightest H_2 knots (see §4.1) detected and the dash-dotted lines correspond to J- and C-shock models from Smith (1995). Sources IR 41, IR 56, IR 58 and IR 93 are labeled to indicate the position of four candidate stars possibly responsible of HH activity in the region (see §5.1). In the lower right corner the average photometric error cross is indicated.

but are in agreement with the theoretical region predicted by Smith (1995) for molecular shocks.

3.3. Extinction

The extinction to individual stars depends on its location in the J-H/H-K diagram. Those in the locus of reddened MS stars are dereddened using the corresponding J/J-H diagram for an adopted distance of 1.8 kpc presented in Fig. 5. While those at positions of reddened CTT and/or Ae/Be stars are dereddened directly in the J-H/H-K diagram, based on their distance to the CTTS line. Each cluster has MS and CTT stars.

The estimated average extinction of the SW cluster is $A_V = 8.44 \pm 4.77$ mag for 18 stars, which excludes the unresolved pair IR 39 with A_V=17.9 and IR 35 which lies $>1\sigma$ below the CTTS line. While, for the NE cluster $A_V = 15.06 \pm 3.48$ mag for 9 stars, excluding IR 58 because this extremely red star has an anomalous extinction, at least twice the average value. IR 58 must be a deeply embedded YSO ($A_V \sim 30.14$ mag) with intrinsic reddening likely produced by a protostellar disk. The mean A_V is assumed for stars IR 93 to IR 97, possible members of the NE cluster. For 40 field stars, i.e. non-cluster stars and associated to S233IR, we obtain $A_V = = 4.88 \pm 4.48$. Due to the uncertainty in distance to S233IR we calculate that the effect on A_V for twice the distance is that the mean value increases by $\sim$8%.

4. Molecular Hydrogen

The molecular hydrogen emission in S233IR is presented in the composite color image in Fig. 2b. H_2 nebulosities are shown in green and clearly stand out from the extended nebulosities shown in Fig. 2a.

4.1. Morphology of H_2 nebulosities

Emission of the molecular hydrogen is mainly associated to six nebular structures shown in Fig. 6, where the continuum subtracted H_2 emission is presented. By comparison with the image in Fig. 2a most of the extended emission at K' is produced by molecular hydrogen. We have designated the H_2 knots or nebulosities as N1 to N6, where the N stands for "nudo" or nebulosity. Detailed contour maps of each H_2 nebulosity show that some consist of several components as is shown in the inserts in Fig. 6. The position, fluxes and sizes of H_2 nebulosities are presented in Table 2.

N1 is the only feature with a clear bow shock morphology pointing North and has two intensity peaks A and B. N1 is also the brighter source detected in H_2 in S233IR. N2 lies very close to N1, located to the South. N2 is more elongated and has also two maxima. Both, N1 and N2 are the only nebulosities for which J, H and K' photometry could be obtained. In Table 1 they correspond to sources IR 81 and IR 77, respectively. Surprisingly, their positions in the J-H/H-K diagram are in agreement with the theoretical region predicted by Smith (1995) for molecular J- and C-shock models (c.f. Fig. 3).

N3 is a chain of small knots linked by weak traces of H_2 gas. Three of them, N3A, N3B and N3C, appear aligned towards IR93 and with the same alignment pattern that H_2O masers trace (Tofani et al. 1995). N4 is a group of three knots around the center of

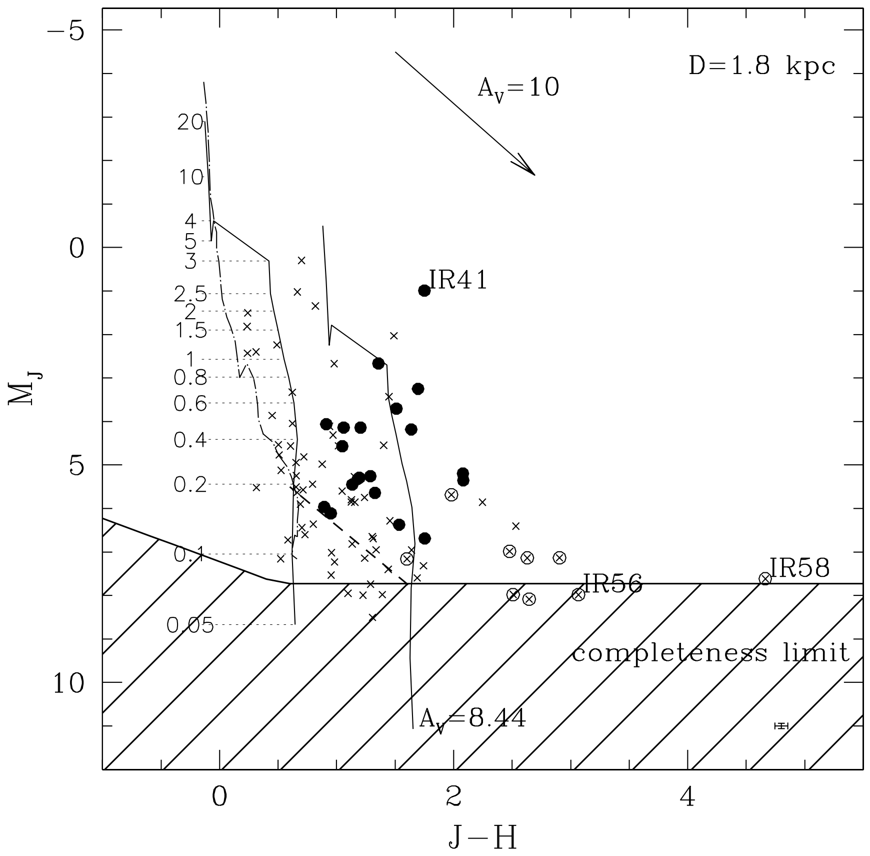

Fig. 5. Color-magnitude diagrams at the adopted D=1.8 kpc (distance modulus 11.28) J vs. J-H. The main sequence is drawn with a dash-dotted line. The solid line represents the 3 Myr isocrone and stellar masses are shown along it (c.f. §5.3). Symbols are the same as in Fig. 3, but arrows were replaced by triangles. Candidate sources IR 41, IR 56, IR 58 and IR 93 are labeled. Completeness limits in magnitude are represented as a dotted line. Extinction vector and average error cross (lower right) are also indicated.

the NE cluster and the stars IR 56, IR 58 and IR 93. N4A is the brightest and extended of the group and also aligned with the chain N3 + IR93 + H_2O maser. H_2O and CH_3OH masers are located in the region between N4A and N4B. This configuration suggests that N3A and N4A are a jet-counter-jet system produced by source IR93.

N5A shows extended and almost spherical emission around the source IR41 which lies closer to the IRAS source position. Several stars in the N5A field did not allow the full detection of this extended nebulosity. It resembles a reflection nebulosity possibly produced by fluorescence (Curiel et al. 1995) instead of shocks. N5B is separated from N5A and located to the NW, possibly aligned with a very weak group of H_2 features. Finally, N6 is an elongated and isolated knot located towards the SE of S233IR, maybe the counter-jet of N1 and N2.

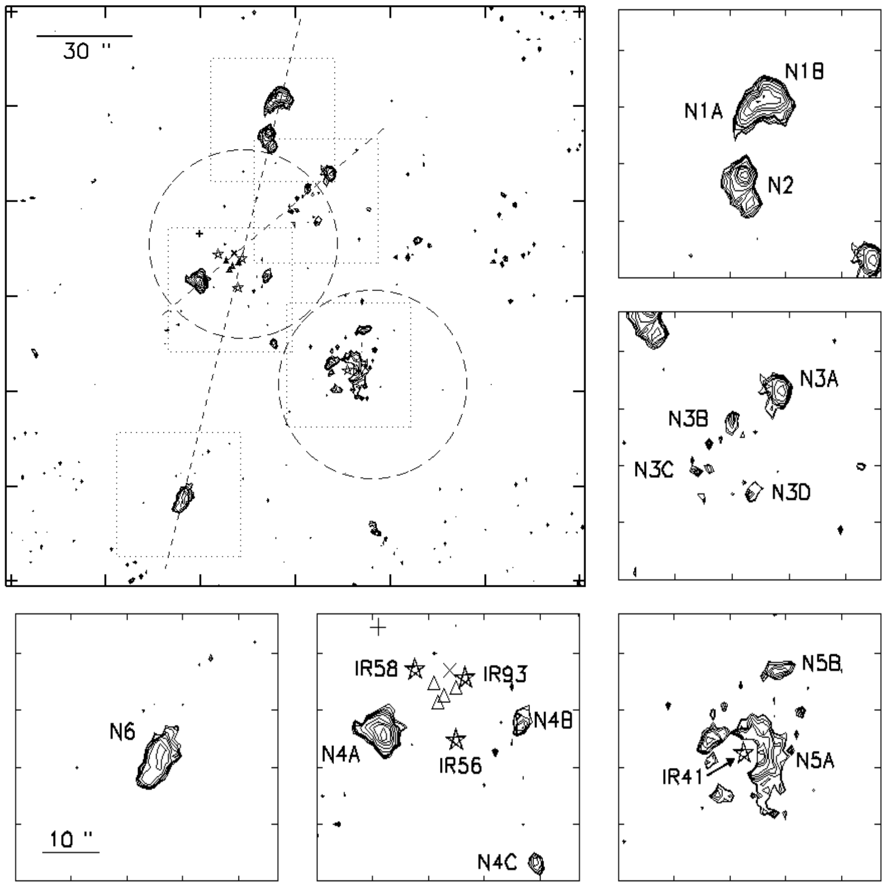

Fig. 6. Contour maps of molecular hydrogen emission. The knots are labeled N1 to N6. Some nebulosities have multiple components labeled A, B, C and D. The scale is presented on the lower left insert. Possible exciting stars ($\star$) and masers of water ($\triangle$), hydroxil ($+$) and methanol ($\times$) are shown.

The positions of knots N1, N2 and N6 describe a line that crosses IR 56 and IR 93, which are the exciting source candidates of these H_2 nebulosities. The morphology and fluxes (Table 2) indicate that they might be part of Herbig-Haro objects in a region of very high extinction, only detectable in the infrared. Radio continuum sources should confirm the nature and location of the exciting source(s). Similar H_2 nebulosities associated to HH objects have been previously discussed (e.g. Lane 1989; Miralles et al. 1997; Zinnecker et al. 1997; Salas et al. 1998; Salas et al. 1999). The association of N4A+N3A and N1+N6 is suggested by the coincidence in exciting source (IR93). We note that most of the H_2 knots are associated with the youngest and reddest cluster, where the GMC core is also located.

4.2. H_2 Velocity Field

The reduction procedure used to obtain images or λ-maps of the region is described in detail in Salas et al. 1999. The velocity corresponding to each channel is referred to the LSR, as all velocities in this paper. The scanning Fabry-Perot images show emission mainly in 5 channels with velocities -36.9 to 2.3 km/s. All the nebulosities show a maximum intensity at velocity channel -17.3 km/s, which is consistent with the GMC rest velocity by Cesaroni et al. 1999 (-15.6 km/s).

The kinematics of the GMC associated to IRAS05358+3543 and the HII regions nearby has been studied in several molecules. Snell et al. 1990 showed that ^{12}CO has weak and extended (ΔV =25 km/s) emission wings. They also found that CO traces two overlapping lobes where both the blue shifted (-30 to -21 km/s) and redshifted (-12 to -6 km/s) emission peaks lie at the position of the IRAS source but no clear bipolar structure. However, this source is usually classified as a bipolar outflow (e.g. Fukui et al. 1993, Wu et al. 1996). Other molecule detections: ACS (2-1) by Bronfman et al. 1996, HCO^+ (1-0) by Richards et al. 1987 and Schreyer et al. 1996 and NH_3 (1,1) and (2,2) (Schreyer et al. 1996), may imply the presence of a massive YSO. The most recent radio study in S233 by Cesaroni et al. 1999 reports several molecular transitions mapped in this region: ^{13}CO(2-1), HCN(1-0), HCO^+(1-0), CS(3-2), $C^{34}S$ (2-1, 3-2 and 5-4). These lines are consistent with an averaged central peak velocity $V_{LSR} \sim$ -15.6 km/s and FWHM$\sim$3.4 km/s. The spectra indicates two velocity components, from -17 to -13.5 km/s and from -20.5 to -17 km/s. These velocity components are consistent with two molecular clumps, one at the H_2O maser position and the other located to the SW, detected in all of the mapped molecular transitions. The exception is $C^{34}S$ which is associated only to the H_2O maser clump, which supports on-going star formation in the denser molecular clump.

The detailed kinematics of H_2 is shown in the individual spectra at the position of the knots, averaged in 3$\times$3 pixel boxes, presented in Fig. 6. The FWHM in the H_2 lines is typically 3 channels (30 km/s), which is wider than the instrumental response (2.4 channels or 23.6 km/s). The observed profiles were fit by Lorentzians which are shown as continuous curves in Fig. 6. The peak velocity and intensity parameters for several knots are presented in cols. (7) and (8) of Table 2. Intensities are given in count/s/channel/pixel and have typical errors of 0.05 in these units, while velocities are given in km/s (LSR) with typical uncertainties of 5 km/s. The velocity of the GMC associated to the H II region S233 reported by Cesaroni et al (1999) is indicated in Fig. 6 as a vertical dotted line. As can be seen from the spectra of 6 H_2 nebulosities: 2 show velocities close to the CO velocity (N2 and N6), 3 are blue-shifted (N1E, N1W and N3A) and N4A is red-shifted.

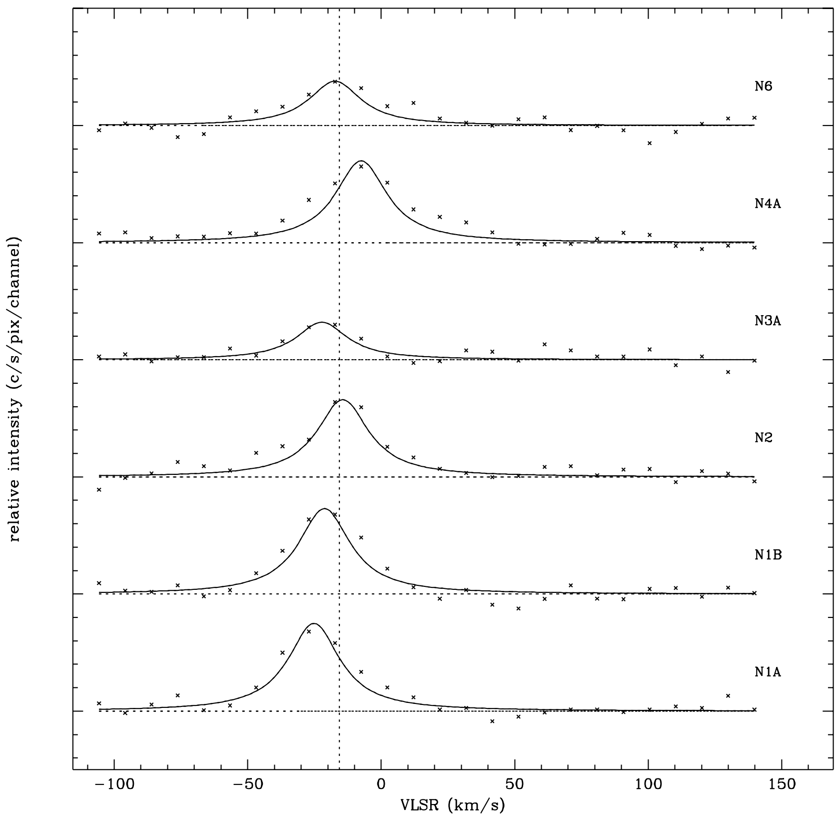

Fig. 7. Velocity components of H_2 knots in the region S233IR, the crosses are the observed relative intensities in units of counts/s/pixel/channel and the continuous line is the Lorentzian fit. The vertical dotted line indicates the ambient CO velocity.

As is shown in Table 2 (c.f. Fig. 2b), knot N1 has a bow shock structure and the two components show similar peak velocities (N1A=-25.2 km/s and N1B=-21.2 km/s), while knots N2 and N6 are slightly redder (-14.4 and -17.3 km/s, respectively) with a velocity consistent with the ambient quiescent medium. The observed velocities reinforce their relation and suggest that they lie on the plane of the sky. The orientation and location of knots N3A (-22.2 km/s) and N4A (-7.5 km/s) suggest that they may form a jet-counter-jet structure oriented to the observers view angle, with knot N4A being the reddest.

The molecular hydrogen nebulosities show velocities consistent with the maser emission peak velocities located near knot N4A (-7.5 km/s): H_2O (-16.9, -17.5, -15.6 and -12.9 km/s; Tofani et al. 1995), CH_3OH (-17 to -10 km/s; Menten 1991) and OH (-11 km/s; Wouterloot et al. 1988). The association between the masers and H_2 nebulosities is reinforced by the similarity in their velocities and are possibly all tracing an outflow/jet emanating from source IR 93 towards knots N4A and N3A.

5. Discussion

5.1. Two Young Stellar Clusters and Molecular Outflow

Evidence for the presence of two distinct YSCs in the S233IR region based on the NIR study are: stellar colors, extinction to NE cluster is ∼7 magnitudes larger than that to the SW cluster, higher population of NIR excess stars in NE cluster, presence of shocked H_2 emission driven by a young star probably associated to the NE cluster. Also, 3 different types of masers are detected in the area of the NE cluster and none associated to de SW cluster. Cesaroni et al. 1999 show that observed molecules trace a core in the H_2O masers positions. Felli et al. 1992 suggest a common energy source for the H_2O maser emission and CO molecular outflows, most probably the stellar wind of a YSO. H_2O and OH maser positions are in agreement with the evolutionary sequence suggested by Forster & Caswell 1989, who suggest that H_2O masers form near the core of a massive protostar while OH masers form in the less dense circumstellar material before the accretion onto the YSO terminates ($\sim 10^5$ years). Menten (1991) identifies the methanol maser (CH_3OH) observed in this region as Class I; and Plambeck & Menten 1990 argue that Class I masers may be formed where molecular outflows shock preexisting dense clumps in a massive star forming region (see Fig. 6). The kinematic association of H_2O masers, the H_2 clumps and the GMC core discussed in §4.2, are all evidence of a molecular outflow emanating from a YSO (possibly IR 93) located in the NE cluster of young stars.

Based on relative positions between stars and H_2 nebulosities, we select four possible candidates as exciting sources of the CO outflow: IR 56, IR 58, IR 93 and IR 41. The HH system composed by knots N1, N2 and N6 has three possible exciting sources; two embedded CTTS IR 56 (A_V = 15.49 mag) and IR 58 ($A_V > 30$ mag), and IR 93 which has no counterpart in the J-filter, is the reddest source in the observed field and has a nebular feature directed in the direction of knots N3 (c.f. Fig. 2). These stars have a steep SED in the NIR. Both IR 56 and IR 93 lie in the path of the line across knots N1, N2 and N6, while IR 58 lies $7''$ to the east. However, the location of masers and GMC core, as well as the kinematical association of the core, masers and H_2 nebulosities, indicate that most probably IR 93 is the exciting source of the molecular outflow. This source is also responsible of the two jet-counter-jet H-H like systems: N1+N6 and N4A+N3A, detected as shocked H_2. A radio continuum study of this region should confirm the location of the exciting source for the molecular outflow and H_2 shocked gas.

IR 41 is located far from the masers and in the SW cluster, most likely associated to IRAS05358+3543 rather than the outflow. Its SED, color and IR-excess indicate that it is a class II Herbig Ae/Be star, according to the classification by Hillenbrand et al. (1992).

It is responsible for the H_2 emission around it (N5A), possibly produced by fluorescence instead of shocks.

5.2. Age estimation

It is not easy to estimate the age of a young stellar cluster without spectroscopic data combined with photometric results. Nevertheless, we can attempt a crude age estimate for a SFR based on a comparison between observed and theoretical luminosity function histograms. The models presented by Zinnecker et al. 1993 and Strom et al. 1993 for K-band and J-band absolute luminosity functions, respectively, provide the necessary KLF and JLF model histograms. Both models are based on the assumption of coeval star formation, use the pre-main sequence isochrones by D'Antona & Mazzitelli (1994) and consider the IMF of Miller & Scalo (1979). The use of JLF is prefered since J provides a more reliable estimate of the true photospheric emission.

Strom et al. 1993 trace six different evolutionary histograms at ages of 0.3, 0.7, 1, 3, 7 and 10 Myr which can be used to construct a matrix $\widehat{M}$ where each column contains the theoretical JLF at each age. Then $\overrightarrow{JLF} = \widehat{M}\ \vec{E}$, where $\overrightarrow{JLF}$ is the J-luminosity function and $\vec{E}$ is defined as an age vector. This matrix is an influence matrix and can be used to estimate an age vector $\vec{E}$ from the observed JLF ($\overrightarrow{JLF}_{obs}$) for each cluster by means of:

$$\vec{E} = (\widehat{M}^T\ \widehat{M})^{-1}\ \widehat{M}\ \overrightarrow{JLF}_{obs}.$$

The elements in $\vec{E}$ give the distribution of cluster stars in all ages and the age estimate can be obtained with the maximum value.

This method is applied to S233IR where we derived $\vec{E}$ for each cluster and field stars. The results are presented in Fig. 8. We fit a parabola to the maximum peak and adjacent points to estimate the following ages: 2.22 Myr for NE cluster, 3.35 Myr for SW cluster, 6.16 Myr for field stars.

Model histograms of JLF at available ages and observed ones are presented in Fig. 9. We can conclude that observed JLF indicate that the NE cluster is younger than the SW cluster.

5.3. Isochrones in the J/J-H diagram

The construction of isochrones in the diagram J/J-H is obtained from pre-main sequence evolutionary tracks by D'Antona & Mazzitelli (1994), assuming Alexander opacities and the Canuto & Mazzitelli convection model, at ages 0.1, 0.3, 1, 3, 10, 30 and 100 Myr. For $M > 2.5\ M_\odot$ we used the tracks presented by Hillenbrand et al. 1995. For each stellar mass M the corresponding luminosity L and effective temperature T_e are obtained.

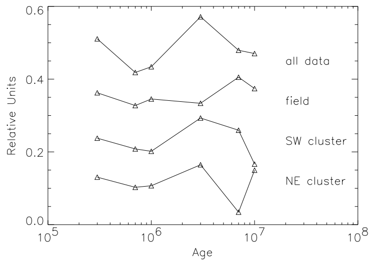

Fig. 8. Age vectors plot for S233IR. Estimated age is obtained from maximum value for field stars, SW cluster and NE cluster.

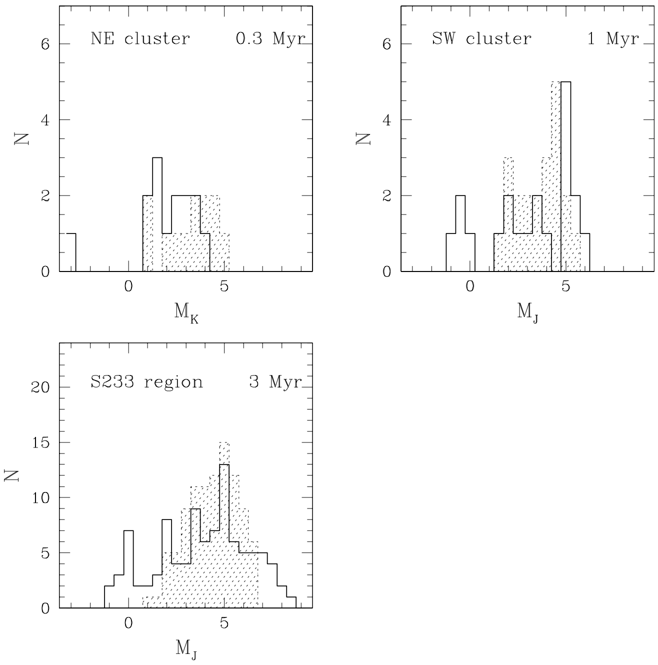

Fig. 9. Observed JLF histograms and the corresponding age for SW cluster, NE cluster and field stars. Shadowed histogram corresponds to the theoretical model by Strom et al. 1993 at 3 Myr.

From L we derive $M_{bol} = 4.74 - 2.5 \ log \ (L/L_{\odot})$ (Bessel et al. 1998) and from T_e the bolometric correction is obtained from Flower (1996), which allows to calculate $M_V = M_{bol} - BC$. Also from T_e, the colors V-J and J-H for dwarfs are obtained from Bessel & Brett (1988), using the T_e values of Tokunaga (2000), Finally, magnitude $J = M_V - (V - J)$. Then PMS isochrones from the HR diagram are transformed to the infrared J/J-H diagram.

In Fig. 5 the isochrone shown corresponds to the estimated age of the SW cluster, along this line the corresponding stellar mass values are clearly indicated. If this isochrone is moved along the extinction vector to the mean value A_V=8.44, we can check the completeness in mass that we are able to detect based on the magnitude limits imposed by our observations. It is clear that stars in the SW cluster of masses from 0.2 to 20 M$\odot$ are detected and only the very low-mass end of dwarf stars is missed. The IMF construction of the SW cluster, presented below, is then justified. This is not the case for the NE cluster, which is deeply embedded (A_V=15.06) and we detect only 4 stars with M from 1 to 20 M$\odot$.

5.4. IMF

The relevance of studying the initial mass function (IMF) in star-forming regions is discussed in a recent review paper by Meyer et al. (2000), hereon MAHCL2000. As they discuss IMF of embedded clusters are fundamental to understand the origin of stellar masses in molecular clouds. The IMF of the region S233IR can be attempted applying a purely photometric technique.

The mass of MS stars can be obtained from the J/J-H diagram using the isochrone for the estimated age of the SW cluster. Reddened stars are de-reddened to the MS of the isochrone and individual masses are obtained.

For stars along the CTT and Ae/Be stars we use the empirical relations from Carpenter et al. 1993:

$$logM_* = -0.24M_K + 0.24 \quad (1)$$

$$logM_* = -0.25M_H + 0.44 \quad (2)$$

where M_H and M_K are the uncorrected for extinction H- and K-band magnitudes, as pointed out by Carpenter et al. 1993. We note that if an A_V of 10 mag is required, this would imply an underestimation of the mass of 0.24 dex for these stars.

We obtained the spectrum of masses for the SW cluster and field stars shown in Fig. 10. The completeness limit in mass estimated for the SW cluster, suggests that the turnover in the IMF for M $<$ 1 $M_\odot$ is probably real. As can be seen the number of intermediate-mass stars in the SW cluster is larger than in field stars. A least squares fit from the peak value to high-mass stars considering stars with M> 1 $M_\odot$ is applied. The slope value ($\Gamma = d\, log\Phi(logM_*)/dlogM_*$) of SW cluster stars is Γ_{SW} = -0.33 $\pm$ 0.21; while for field stars Γ_{field} = -1.07 $\pm$ 0.53. As suggested by MAHCL2000 the best diagnostics in YSCs is the ratio R of intermediate-to-low-mass stars, $R = N(1-10M_\odot)/N(0.1-1M_\odot)$ (c.f. Fig 3 and Table 1 in MAHCL2000). For the SW cluster we obtained $R = 0.73$ somewhat larger than the values presented by MAHCL2000, and $R = 0.24$ for field stars, consistent with Miller & Scalo (1979) IMF according to MAHCL2000. For the NE cluster we detect 6 low-mass stars deeply embedded, while on the high-mass we detect only 3, which implies that $R < 0.5$. However, spectroscopic follow-up in S233IR is required to estimate stellar temperatures and a reliable estimation of the stellar IMF.

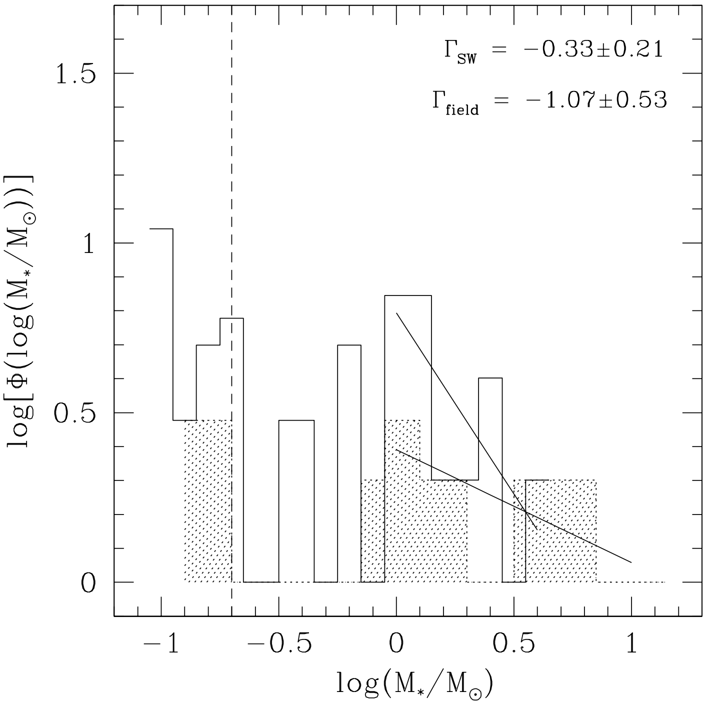

Fig. 10. IMF histogram of the SW cluster (shadowed) and field stars (empty) in the S233IR region. Slope values (Γ) obtained for M≥1 $M_\odot$ are given on top. The dotted vertical line represents the completeness limit in mass for the SW cluster, for field stars this limit is slightly to the left.

6. Conclusions

1. Direct J, H and K' images and photometric results of the S233IR reveal the existence of two young embedded clusters near IRAS05358+3543. Average extinction values are $A_V = 9.36 \pm 2.67$ mag and $A_V = 14.19 \pm 2.23$ mag for the SW and NE clusters, respectively. The separation between clusters is about 0.5 pc at the adopted distance of 1.8 kpc.

2. Emission from molecular hydrogen is mainly associated to six nebular structures most likely produced by shocks with similar properties as deeply embedded Herbig-Haro objects. Most of them are directly associated to the NE cluster, where several tracers of star formation activity are located.

3. The presence of young stars, molecular outflow, GMC core and masers related with the NE cluster, as well as the presence of HH-like activity and cluster members colors, strongly suggest that the NE cluster is younger than the SW cluster. At least two star-formation episodes are revealed by our study.

4. The H_2 emission velocity field and peak velocities are consistent with the GMC rest velocity and H_2O maser peak velocities. Morphology and velocities show that two jet-counter-jet structures produced by shocks with properties similar to deeply embedded

Herbig-Haro objects are present in the field. Nebulosity N6 is the redder part of a bipolar jet emanating from the center of the NE cluster, while N1 (bow shock structure) and N2 are the bluer counterpart. While H_2 nebulosities N4A and N3A trace another jet-counter-jet.

5. A group of candidates stars responsible for H_2 emission is considered. IR 41 related with IRAS05358+3543 and associated to the bluer cluster (SW) seems to be the exciting source of fluorescence H_2 emission around it. While most probably IR 93, located near the center of the NE cluster produces the molecular outflow emission and HH activity in the S233IR region. Radio continuum studies are needed to locate the outflow/jet source and its association to IR 93.

6. Luminosity function histograms are used to obtain a crude age estimation of each cluster, 1 Myr for the SW and 0.3 Myr for the NE.

7. IMF slopes of cluster members (Γ_C = -0.47 $\pm$ 0.17) and field + cluster stars (Γ_{all} = -0.85 $\pm$ 0.17) are flatter than Salpeter's value (-1.35, Salpeter 1955).

hich can be compared to the Salpeter's value of -1.35 (Salpeter 1955).

Acknowledgements. Arbitro We are debted to L. Georgiev our IDL guru... We thank the OAN/SPM night assistants E. García, F. Montalvo and S. Monroy and the OAN/SPM technical support group for their valuable help during the observations. This work has been financed by grant IN-501694 and IN-120198 from DGAPA (UNAM). A. Porras has been supported by a CONACYT (México) scholarship. Finally, we thank A. Sobolev for his comments.

References

Bessell, M. S., Brett, J. M., 1988, PASP 100, 1134.

Bessell, M.S., Castelli, F., Plez, B. 1998, A&A 333, 231.

Bronfman, L., Nyman, L.-A., May, J., 1996, A&AS 115, 81.

Carpenter, J.M., Snell, R.L., Schloeb, F.P., Skrutskie, M.F., 1993, ApJ 407, 657.

Carpenter, J.M., Meyer, M.R., Dougados, C., Strom, S.E., Hillenbrand, L.A., 1997, AJ 114, 198.

Carrasco, L., Recillas-Cruz, E., García-Barreto, A., Cruz-González, I., Serrano, A., 1991, PASP 103, 987.

Casoli, F., Combes, F., Dupraz, C., Gerin, M., Boulanger, F., 1986, A&A 169, 281.

Caswell, J.L., Vaile, R.A., Forster, J.R., 1995, MNRAS 277, 210.

Cesaroni, R., Felli, M., Walmsley, C.M., 1999, A&AS 136, 333.

Cruz-González, I., Carrasco, L., Ruiz, E., et al., 1994, CAMILA: Infrared Camera/Spectrograph for OAN/SPM. In: "Instrumentation in Astronomy VIII", D.L. Crawford & E.R. Craine (eds.) Proc. SPIE 2198, 774.

Curiel, S., Raymond, J.C., Wolfire, M., Hartigan, P., Morse, J., Schwartz, R.D., Nisenson, P., 1995, ApJ 453, 322.

Chan, G., Fich, M., 1995, AJ 109, 2611.

Chan, S.J., Henning, T., Schreyer, K., 1996, A&AS 115, 285.

D'Antona, F., Mazzitelli, I., 1994, ApJS 90, 467.

Evans, N.J. II, Blair, G.N., 1981, ApJ, 246, 394.

Felli, M., Palagi, F., Tofani, G., 1992, A&A 255, 293.

Fich, M., Blitz, L., 1984, ApJ 279, 125.

Flower, P.J., 1996, ApJ 469, 355.

Forster, J.R., Caswell, J.L., 1989, å 213, 339.

Fukui, Y., Iwata, T., Mizuno, A., Bally, J., Lane, A.P., 1993, Molecular Outflows. In: Protostars and Planets III, ed. E.H. Levy & J.I. Lunine (eds.), (Tucson: University of Arizona Press), p. 603.

Henning, T., Cesaroni, R., Walmsley, M., Pfau, W., 1992, A&AS 93, 525.

Heyer, M.H., Carpenter, J.M., Ladd, E.F., 1996, ApJ 463, 630.

Hillenbrand, L. A., Strom, S. E., Vrba, F. J., Keene, J., 1992, ApJ 397, 613.

Hillenbrand, L. A., Meyer, M.R., Strom, S.E., Skrutskie, M.F., 1995, AJ 109, 280.

Hodapp, K.-W., 1994, ApJS 94, 615.

Hughes, V.A., MacLeod, G.C., 1989, AJ 97, 786.

Israel, F.P., Felli, M., 1978, A&A 63, 325.

Landsman, W. B., 1996, IDL Astronomy User's Library. In: http: //idlastro.gsfc.nasa.gov /homepage.html

Lane, A. P., 1989. Near-Infrared Imaging of H_2 Emission from Herbig-Haro Objects and Bipolar Flows. In: Proc. ESO Workshop on Low Mass Star Formation and Pre-Main Sequence Objects, Reipurth B. (ed.) (Garching: ESO), 331.

Menten, K.M., 1991, ApJ 380, L75.

Meyer, M. R., 1996, Ph.D. Thesis, University of Massachusetts.

Meyer, M. R., Adams, F.C., Hillendrand, L.A., Carpenter, J.M., Larson, R.B., 2000, The Stellar Initial Mass function: Constraints from Young Clusters and Theoretical Perspectives. In: Protostars and Planets IV, Mannings V. , Boss A.P. & Rusell S.S. (eds.), in press.

Miller, G.E., Scalo, J.M., 1979, ApJS 41, 513.

Miralles, M., Salas, L., Cruz-González, I., Kurtz, S., 1997, ApJ 488, 749.

Palagi, F., Cesaroni, R., Comoretto, G., Felli, M., Natale, V., 1993, A&A 101, 153.

Plambeck, R. L., Menten, K. M., 1990, ApJ 364, 555.

Porras, A., 2000, Ph.D. Thesis (in preparation).

Porras, A., Cruz-González, I., Salas, L., 2000, (in preparation)

Richards, P.J., Little, L.T., Heaton, B.D., Toriseva, M., 1987, MNRAS 228, 43.

Salas, L., Cruz-González, I., Porras, A., 1998, ApJ 500, 853.

Salas, L., Rosado, M., Cruz-González, I., Gutiérrez L., Valdez, J., Bernal, A., Luna, E., Ruiz, E., Lazo, F., 1999, ApJ 511, 822.

Salpeter, E.E., 1955, ApJ 121, 161.

Schreyer, K., Henning, T., Koempe, C., Harjunpaeae, P., 1996, A&A 306, 267.

Sharpless, S., 1959, ApJS 4, 257.

Smith, M. D., 1995, A&A 296, 789.

Snell, R.L., Dickman, R.L., Huang, Y.-L., 1990, ApJ 352, 139.

Strom, K.M., Strom, S.E., Merrill, M., 1993, ApJ 412, 233.

Tofani, G., Felli, M., Taylor, G.B., Hunter, T.R., 1995, A&AS 112, 299.

Tokunaga, A.T. 2000, Infrared Astronomy. In: Allen's Astrophysical Quantities, Cox, A.N. (ed.), (New York: Springer-Verlag), p. 143.

Wilking, B.A., Blackwell, J.H., Mundy, L.G., Howe, J.E., 1989, ApJ 345, 257.

Wood, D.O.S., Churchwell, E., 1989, ApJ 340, 265.

Wouterloot, J.G.A., Henkel, C., Brand, J., 1988, A&A 191, 323.

Wouterloot, J.G.A., Brand, J., 1989, A&AS 80, 149.

Wu, Y., Huang, M., He, J., 1996, A&AS 115, 283.

Zinnecker, H., Mc Caughrean, M.J., Wilking, B.A., 1993, The Initial Stellar Population. In: Protostars and Planets III, Levy E.H., Lunine J.I. (eds.) (Tucson: University of Arizona Press), p. 429.

Zinnecker, H., Mc Caughrean, M., Rayner, J., 1997, HH212: a prototype molecular hydrogen jet from a deeply embedded protostar. In: Low Mass Star Formation - from Infall to Outflow, poster proceedings of IAU Symp. 182, Malbet F., Castets A. (eds.), p. 198.

Table 1. Infrared Sources in the S233IR Region

Source (1)	α_{1950} (2)	δ_{1950} (3)	J (4)	H (5)	K (6)	A_V (7)
IR 1 [1]	05 35 52.1	+35 42 34.2	15.14 ± 0.04	14.69 ± 0.06	14.39 ± 0.07	—
IR 2 [1]	05 35 51.8	+35 42 39.1	13.95 ± 0.02	12.97 ± 0.04	12.62 ± 0.05	8.28 [5]
IR 3 [1]	05 35 49.5	+35 42 34.9	15.59 ± 0.01	14.62 ± 0.02	14.17 ± 0.07	5.85 [5]
IR 4	05 35 46.7	+35 42 36.5	17.64 ± 0.06	16.84 ± 0.04	16.17 ± 0.10	—
IR 5	05 35 45.1	+35 42 43.1	18.09 ± 0.12	16.96 ± 0.05	16.34 ± 0.11	2.03 [4]
IR 6 [1]	05 35 47.6	+35 42 44.4	11.58 ± 0.02	10.87 ± 0.03	10.30 ± 0.06	—
IR 7 [1]	05 35 52.6	+35 42 48.2	15.84 ± 0.01	15.23 ± 0.02	15.25 ± 0.09	2.18 [5]
IR 8	05 35 52.8	+35 42 52.7	18.60 ± 0.10	16.85 ± 0.06	16.34 ± 0.18	11.85 [5]
IR 9 [1,11]	05 35 53.0	+35 42 58.5	16.22 ± 0.01	15.57 ± 0.02	15.26 ± 0.10	1.67 [5]
IR 10	05 35 48.6	+35 42 50.1	15.84 ± 0.02	14.82 ± 0.04	14.38 ± 0.06	6.65 [5]
IR 11	05 35 44.5	+35 42 51.2	17.13 ± 0.07	16.00 ± 0.04	15.63 ± 0.09	6.68 [5]
IR 12 [1,11]	05 35 42.365	+35 42 51.64	12.78 ± 0.02	12.54 ± 0.04	12.44 ± 0.07	1.29 [5]
IR 13	05 35 53.9	+35 42 54.2	19.78 ± 0.24	18.47 ± 0.14	17.29 ± 0.20	0.00 [4]
IR 14	05 35 46.6	+35 42 54.1	18.81 ± 0.14	17.85 ± 0.08	17.05 ± 0.14	—
IR 15 [3]	05 35 47.5	+35 43 47.6	16.92 ± 0.04	15.59 ± 0.06	14.64 ± 0.08	1.89 [4]
IR 16	05 35 49.4	+35 43 0.6	18.23 ± 0.09	16.59 ± 0.04	15.42 ± 0.07	4.16 [4]
IR 17 [1]	05 35 44.1	+35 43 03.6	12.62 ± 0.02	11.80 ± 0.03	11.76 ± 0.04	7.69 [5]
IR 18 [11]	05 35 50.9	+35 43 03.8	17.72 ± 0.05	17.01 ± 0.05	16.66 ± 0.08	0.72 [5]
IR 19 [3]	05 35 47.7	+35 43 09.4	16.73 ± 0.05	15.59 ± 0.04	15.02 ± 0.08	7.34 [5]
IR 20 [3]	05 35 48.0	+35 43 09.1	15.34 ± 0.02	14.43 ± 0.02	14.14 ± 0.06	6.68 [5]
IR 21 [3]	05 35 45.9	+35 43 16.1	15.42 ± 0.02	14.22 ± 0.02	13.69 ± 0.11	10.37 [5]
IR 22 [11]	05 35 51.2	+35 43 13.2	17.88 ± 0.06	17.15 ± 0.08	16.87 ± 0.14	0.30 [5]
IR 23 [1]	05 35 51.4	+35 43 19.7	17.68 ± 0.07	15.15 ± 0.03	14.16 ± 0.04	21.42 [5]
IR 24 [1]	05 35 51.7	+35 43 20.3	14.60 ± 0.01	13.98 ± 0.02	14.00 ± 0.04	4.12 [5]
IR 25 [3]	05 35 47.1	+35 43 14.3	16.60 ± 0.03	15.42 ± 0.02	14.86 ± 0.06	8.34 [5]
IR 26 [3]	05 35 46.8	+35 43 15.8	17.39 ± 0.06	16.44 ± 0.05	15.69 ± 0.10	0.00 [4]
IR 27	05 35 55.1	+35 43 16.5	16.91 ± 0.03	16.24 ± 0.04	15.57 ± 0.16	—
IR 28	05 35 55.4	+35 43 16.4	17.02 ± 0.04	15.78 ± 0.02	15.11 ± 0.11	2.97 [4]
IR 29 [3]	05 35 47.5	+35 43 21.4	16.54 ± 0.05	15.25 ± 0.06	14.82 ± 0.08	9.10 [5]
IR 30 [3]	05 35 47.6	+35 43 24.7	15.41 ± 0.02	14.35 ± 0.04	14.01 ± 0.06	8.20 [5]
IR 31 [3]	05 35 47.3	+35 43 27.9	14.98 ± 0.02	13.47 ± 0.03	12.85 ± 0.04	12.71 [5]
IR 32 [3]	05 35 48.0	+35 43 27.6	14.52 ± 0.02	12.83 ± 0.03	12.07 ± 0.04	14.48 [5]
IR 33 [3]	05 35 47.3	+35 43 32.5	17.65 ± 0.12	16.11 ± 0.10	15.34 ± 0.10	10.59 [5]
IR 34	05 35 44.1	+35 43 23.1	19.26 ± 0.20	17.87 ± 0.12	17.09 ± 0.11	4.02 [4]
IR 35 [3]	05 35 46.3	+35 43 31.0	17.24 ± 0.03	16.35 ± 0.13	15.38 ± 0.06	~8.44 [8]
IR 36 [3]	05 35 46.8	+35 43 31.1	16.57 ± 0.02	15.37 ± 0.06	14.42 ± 0.06	0.22 [4]
IR 37	05 35 55.8	+35 43 23.6	17.13 ± 0.02	15.98± 0.02	15.10 ± 0.08	0.41 [4]
IR 38 [3]	05 35 48.8	+35 43 25.2	13.94 ± 0.03	12.59 ± 0.03	12.07 ± 0.05	11.56 [5]
IR 39 [3]	05 35 48.5	+35 43 29.8	16.47 ± 0.11	14.39 ± 0.07	14.11 ± 0.11	17.89 [5,9]

Table 1. Continued

Source	α_{1950}	δ_{1950}	J	H	K	A_V
(1)	(2)	(3)	(4)	(5)	(6)	(7)
IR 40 [3]	05 35 48.8	+35 43 34.8	16.63 ± 0.13	14.55 ± 0.12	13.85 ± 0.08	17.71 [5]
IR 41 [3,6]	05 35 48.3	+35 43 39.0	12.27 ± 0.02	10.52 ± 0.05	9.36 ± 0.11	5.52 [4]
IR 42 [3]	05 35 50.0	+35 43 31.0	15.85 ± 0.02	14.80 ± 0.03	14.26 ± 0.06	6.72 [5]
IR 43 [1]	05 35 53.2	+35 43 35.6	13.09 ± 0.02	12.86 ± 0.03	12.97 ± 0.06	2.19 [5]
IR 44 [3]	05 35 49.7	+35 43 44.5	15.46 ± 0.02	13.82 ± 0.02	13.39 ± 0.06	13.64 [5]
IR 45	05 35 44.6	+35 43 40.4	18.87 ± 0.17	17.18 ± 0.07	16.75 ± 0.09	9.04 [5]
IR 46	05 35 42.9	+35 43 50.5	15.390 ± 0.03	14.45 ± 0.06	14.02 ± 0.04	6.87 [5]
IR 47	05 35 43.6	+35 43 45.6	19.23 ± 0.20	18.13 ± 0.16	17.26 ± 0.17	0.00 [4]
IR 48	05 35 51.8	+35 43 44.6	14.71 ± 0.02	13.26 ± 0.02	12.82 ± 0.03	11.80 [5]
IR 49	05 35 53.1	+35 43 45.9	15.82 ± 0.03	14.42 ± 0.03	13.61 ± 0.04	3.90 [4]
IR 50	05 35 45.1	+35 43 46.8	17.08 ± 0.06	15.95 ± 0.04	15.28 ± 0.07	1.58 [4]
IR 51	05 35 45.4	+35 43 47.4	17.92 ± 0.11	16.62 ± 0.06	15.63 ± 0.08	1.35 [4]
IR 52 [1,11]	05 35 44.6	+35 43 49.3	13.71 ± 0.02	13.47 ± 0.02	13.37 ± 0.06	0.96 [5]
IR 53	05 35 42.2	+35 43 49.6	17.97 ± 0.07	16.65 ± 0.04	15.76 ± 0.08	2.21 [4]
IR 54 [3]	05 35 46.4	+35 43 49.5	17.97 ± 0.06	16.22 ± 0.05	15.23 ± 0.07	6.86 [4]
IR 55 [2]	05 35 50.4	+35 44 04.5	16.96 ± 0.03	14.98 ± 0.03	14.42 ± 0.09	15.97 [5]
IR 56 [2]	05 35 51.2	+35 44 05.1	19.26 ± 0.22	16.19 ± 0.03	14.22 ± 0.09	15.51 [4]
IR 57	05 35 44.6	+35 44 10.8	13.30 ± 0.01	11.82 ± 0.03	11.64 ± 0.05	13.64 [5]
IR 58 [2]	05 35 51.7	+35 44 15.7	18.89 ± 0.15	14.23 ± 0.07	11.60 ± 0.12	30.14 [4]
IR 59 [2]	05 35 52.0	+35 44 22.5	19.36 ± 0.21	16.72 ± 0.14	15.25 ± 0.19	14.18 [4]
IR 60 [2]	05 35 52.4	+35 44 23.9	19.25 ± 0.19	16.75 ± 0.14	15.03 ± 0.16	10.65 [4]
IR 61	05 35 55.5	+35 44 14.6	18.42 ± 0.10	17.18 ± 0.05	16.28 ± 0.08	1.25 [4]
IR 62 [2]	05 35 53.2	+35 44 23.8	18.41 ± 0.10	15.78 ± 0.06	14.34 ± 0.08	14.13 [4]
IR 63	05 35 55.2	+35 44 21.8	16.80 ± 0.03	16.48 ± 0.03	15.96 ± 0.07	—
IR 64 [1]	05 35 56.6	+35 44 30.9	12.30 ± 0.01	11.63 ± 0.03	11.66 ± 0.06	5.77 [5]
IR 65 [2]	05 35 50.9	+35 44 31.6	18.26 ± 0.07	15.78 ± 0.04	14.57 ± 0.06	20.49 [5]
IR 66 [2]	05 35 52.3	+35 44 39.8	18.44± 0.07	16.84 ± 0.05	16.03 ± 0.09	9.50 [5]
IR 67	05 35 55.7	+35 44 35.4	18.00 ± 0.09	17.42 ± 0.07	16.70 ± 0.13	—
IR 68	05 35 56.1	+35 44 39.2	19.02 ± 0.19	17.73 ± 0.09	16.79 ± 0.16	1.57 [4]
IR 69	05 35 42.4	+35 44 33.9	19.27 ± 0.19	18.04 ± 0.13	16.73 ± 0.24	—
IR 70 [11]	05 35 46.1	+35 44 37.2	16.52 ± 0.03	15.87 ± 0.03	15.58 ± 0.09	0.70 [5]
IR 71 [2]	05 35 50.0	+35 44 43.9	18.41 ± 0.12	15.51 ± 0.03	13.93 ± 0.08	16.57 [4]
IR 72 [2,10]	05 35 49.7	+35 44 49.1	17.13 ± 0.04	14.89 ± 0.03	13.88 ± 0.09	18.56 [5]
IR 73	05 35 43.9	+35 44 48.7	17.18 ± 0.03	16.48 ± 0.04	15.70 ± 0.15	—
IR 74	05 35 52.1	+35 44 51.2	18.23 ± 0.05	16.89 ± 0.05	16.27 ± 0.10	6.66 [5]
IR 75	05 35 52.4	+35 44 55.3	16.88 ± 0.02	15.83 ± 0.02	15.48 ± 0.07	5.84 [5]
IR 76	05 35 52.0	+35 45 00.3	16.72 ± 0.02	15.92 ± 0.03	15.37 ± 0.09	—
IR 77/N2	05 35 50.4	+35 44 54.0	18.68 ± 0.11	17.24 ± 0.07	15.33 ± 0.06	—
IR 78	05 35 46.9	+35 45 08.1	16.40 ± 0.02	15.87 ± 0.03	15.32 ± 0.14	—

Table 1. Continued

Source	α_{1950}	δ_{1950}	J	H	K	A_V
(1)	(2)	(3)	(4)	(5)	(6)	(7)
IR 79	05 35 52.652	+35 45 2.34	16.55 ± 0.05	15.40 ± 0.02	14.93 ± 0.04	8.15 [5]
IR 80 [1]	05 35 53.1	+35 45 5.2	13.68 ± 0.02	13.36 ± 0.01	13.40 ± 0.05	2.06 [5]
IR 81/N1	05 35 50.0	+35 45 05.7	18.43 ± 0.08	17.91 ± 0.17	15.87 ± 0.20	—
IR 82	05 35 54.9	+35 45 5.4	18.50 ± 0.11	17.52 ± 0.07	16.48 ± 0.20	—
IR 83	05 35 44.0	+35 45 12.1	16.78 ± 0.03	16.13 ± 0.04	15.61 ± 0.13	—
IR 84 [1]	05 35 49.2	+35 45 11.4	15.81 ± 0.02	15.31 ± 0.02	15.16 ± 0.10	0.26 [5]
IR 85	05 35 57.1	+35 45 17.4	16.85 ± 0.05	16.13 ± 0.04	15.77 ± 0.08	1.76 [5]
IR 86	05 35 52.0	+35 45 28.8	16.09 ± 0.01	15.37 ± 0.02	15.03 ± 0.07	3.06 [5]
IR 87	05 35 55.6	+35 45 24.2	16.04 ± 0.02	15.54 ± 0.05	15.10 ± 0.07	—
IR 88 [1]	05 35 42.3	+35 45 28.9	13.52 ± 0.02	13.03 ± 0.02	13.00 ± 0.05	3.78 [5]
IR 89	05 35 48.7	+35 45 29.5	17.56 ± 0.04	16.10 ± 0.017	15.69 ± 0.23	10.23 [5]
IR 90	05 35 50.5	+35 45 30.3	18.29 ± 0.08	17.34 ± 0.08	16.65 ± 0.12	0.00 [4]
IR 91 [1]	05 35 55.1	+35 45 30.9	15.32 ± 0.02	14.70 ± 0.02	14.47 ± 0.06	3.82 [5]
IR 92	05 35 55.5	+35 45 33.6	16.26 ± 0.03	15.38 ± 0.03	14.88 ± 0.07	0.00 [4]
IR 93 [2]	05 35 51.1	+35 44 14.4	—	16.09 ± 0.12	12.96 ± 0.19	∼15.06 [7]
IR 94 [2]	05 35 51.7	+35 44 11.5	—	15.91 ± 0.13	13.41 ± 0.11	∼15.06 [7]
IR 95 [2]	05 35 52.5	+35 44 08.5	—	16.69 ± 0.09	14.78 ± 0.18	∼15.06 [7]
IR 96 [2]	05 35 53.2	+35 44 1.7	—	16.02 ± 0.03	14.05 ± 0.07	∼15.06 [7]
IR 97 [2]	05 35 50.0	+35 43 53.38	—	17.03 ± 0.07	15.12 ± 0.09	∼15.06 [7]
IR 98	05 35 50.6	+35 43 37.5	—	16.64 ± 0.06	14.53 ± 0.05	∼15.06 [7]

[1] Star with optical counterpart.
[2] NE cluster member
[3] SW cluster member
[4] CTT star with near-IR excess emission de-reddened in the J-H/H-K diagram
[5] star with reddened main sequence colors de-reddened in the J/J-H diagram
[6] Source IRAS05358+3543
[7] Average extinction of NE cluster
[8] Average extinction of SW cluster
[9] Unresolved pair of stars, magnitudes and A_V refer to pair
[10] Star at edge of cluster radius, most likely also a member of NE cluster.
[11] Foreground star.

Table 2. Properties of Molecular Hydrogen Nebulosities in the S233IR Region

Source	α_{1950}	δ_{1950}	I_{max} [1]	$Flux$ [2]	Size [3]	I^V_{peak} [4]	V_{peak} [5]
(1)	(2)	(3)	(4)	(5)	(6)	(7)	(8)
N1A	05 35 50.07	+35 45 05.66	1.04	7.92	6.7 × 5.0	0.75	-25.2
N1B	05 35 50.07	+35 45 05.66	1.04	7.92	6.7 × 5.0	0.73	-21.2
N2	05 35 50.41	+35 44 54.02	0.82	4.57	4.2 × 6.7	0.66	-14.4
N3A	05 35 48.81	+35 44 41.38	0.54	2.82	5.0 × 4.2	0.32	-22.2
N3B	05 35 49.35	+35 44 35.65	0.40	1.02	4.2 × 2.5		
N3C	05 35 49.70	+35 44 29.00	0.38	0.91	4.2 × 2.5		
N3D	05 35 49.23	+35 44 26.53	0.42	0.64	3.4 × 1.7		
N4A	05 35 51.69	+35 44 15.59	1.00	5.59	5.0 × 4.2	0.7	-7.5
N4B	05 35 50.49	+35 44 08.55	0.43	0.72	2.5 × 2.5		
N4C	05 35 50.25	+35 43 47.99	0.37	1.01	3.4 × 3.4		
N5A	05 35 52.58	+35 42 58.87	0.53	12.07	12.6 × 15.12		
N5B	05 35 47.89	+35 43 51.59	0.49	1.08	3.4 × 2.5		
N6	05 35 52.64	+35 42 58.35	0.73	3.83	4.2 × 5.0	0.38	-17.3

[1] Peak intensity in units of 10^{-4} erg s^{-1} cm^{-2} sr^{-1}

[2] Total flux in units of 10^{-14} erg s^{-1} cm^{-2}

[3] Size in arcsec

[4] Peak intensity of Lorentzian fit in units of count/s/channel/pixel

[5] Peak velocity of Lorentzian fit (LSR) in km/s

List of Objects